Vibration energy analysis of a plate for defect imaging with a scanning laser source technique

Takahiro Hayashi[a] and Misaki Fukuyama
Graduate School of Engineering, Kyoto University, Kyoto 615-8540, Japan

(Received 6 April 2016; revised 24 July 2016; accepted 12 September 2016; published online 7 October 2016)

Vibration energies generated by laser irradiation to a plate with a crack were calculated by the semi-analytical finite element method to elucidate the principle of defect imaging using a scanning laser source. For normal incidence in the ablation regime, the incident energy increases when the incident source is located in the vicinity of the crack, owing to the effect of the non-propagating A1 modes. For dipole loading in the thermoelastic regime, the vibration energies are completely different, depending on the position of the crack opening. If the crack opening is located opposite the incident source, the vibration energy increases abruptly in the vicinity of the crack, which is affected by the higher-order non-propagating modes as well as the A1 modes. When the crack opening and the incident source are located on the same side, the generated energy approaches zero as the source moves closer to the crack. The energy reduction around the crack is caused by the superposition of the incident wave from dipole loading and the phase-inverted reflected wave. The results of experiments conducted to verify the energy variations in the vicinity of a crack were in good agreement with the numerical results for dipole loading.
 [http://dx.doi.org/10.1121/1.4964275]

[NJK] Pages: 2427–2436

I. INTRODUCTION

Guided waves are often used to inspect large plate-like structures, such as pipes, tanks, and airplane bodies and wings,[1–12] owing to such waves' prominent characteristic of long-range propagation. In most cases, rapid long-range inspections are conducted by measuring guided waves reflected or transmitted by defects. However, the defect detection sensitivity decreases as the frequency decreases and the wavelength increases; hence, echo signals from defects of a desired size cannot be measured when a low-frequency band with smaller attenuation is used for long-range propagation. Defect imaging techniques that use such guided wave signals need to achieve a trade-off between long-range propagation and sufficient image resolution.[8–12]

The authors have studied defect imaging using a scanning laser source (SLS) technique as a new and efficient imaging method for inspecting plate-like structures.[13–18] The SLS technique is a measurement technique in which a laser source of elastic waves is scanned over a plate-like structure, and a large number of waveforms are detected for a large number of wave sources. Kromine *et al.*[19] and Sohn and Krishnaswamy[20,21] showed that surface breaking flaws can be detected with high sensitivity by observing changes in the amplitude and frequency of Rayleigh waves generated using the SLS technique. Dixon *et al.*[22] and Clough and Edwards[23,24] observed an increase in amplitude when a laser source was located in the vicinity of notches in a plate. Using the SLS technique, Fomitchov *et al.*[25] obtained B-scan images of defects in sandwich specimens composed of graphite–epoxy face sheets with a PVC core. Takatsubo *et al.*[26] created an animation of wave propagation on an object surface from a large number of waveforms measured by the SLS technique and evaluated defects from the distortions in wave propagation. The authors demonstrated experimentally and numerically that the plate thickness distribution can be obtained from amplitude distributions measured using the SLS technique in a low-frequency range below the A1 cutoff frequency. Images of notch-type defects in a plate were obtained using similar measurements.[14–16] Recently, the authors successfully developed a rapid non-contact imaging system consisting of fiber laser equipment for generating narrow-band burst waves with a high signal level in the frequency domain and a laser Doppler vibrometer for non-contact detection.[17,18] The authors also examined the effect of quick measurements on the images and demonstrated the potential for creating a defect image within a few seconds. This imaging technique provides high detection sensitivity, as in the studies described above,[18–23] non-contact measurements from a few meters, and fast defect imaging. Therefore, it can be implemented as a camera, using elastic waves, i.e., an E-camera.

In this study, Lamb wave energy propagation in the cross section of a plate was examined to elucidate the principle and evaluate the potential of the E-camera. The semi-analytical finite element (SAFE) method,[27–34] an efficient calculation technique for guided waves, was used in the numerical analyses. Propagation energy in a plate is discussed in this paper using the velocity vectors and stress tensors in the SAFE formulation, and elastic wave energy generated in a plate with a crack is discussed using the calculation results. The SLS technique was used to obtain images of defects located on the same side and the opposite side of a

[a]Electronic mail: hayashi@kuaero.kyoto-u.ac.jp

laser source, and the calculation results for the energy variations were validated using the experimental results.

II. CALCULATION OF CROSS-SECTIONAL ENERGY USING THE SAFE METHOD

The SAFE method is a specialized version of the finite element method for elongated structures with uniform geometries and material constants in the longitudinal direction.[27–34] Because this technique requires only division of the cross section of a bar-like structure, guided wave propagation can be carried out more efficiently than in the case of general finite element analysis, which requires a whole region to be divided into small elements. Moreover, the SAFE method is suitable for modal analysis because wave fields in a bar-like structure are expressed as the sum of guided wave modes.

We consider Lamb waves vibrating in the x–y plane and propagating in the longitudinal direction (the $\pm x$ direction) in a thin plate with traction-free boundaries, as shown in Fig. 1. Analytical solutions for this case are given by normal mode expansion, which yields a velocity vector at an arbitrary point on the cross section of the plate in the form of the summation of the eigenmodes of the Lamb waves for a harmonic vibration with angular frequency ω,[1,2,35,36]

$$\mathbf{v} = \sum_m \alpha_m \mathbf{v}_m \exp\left(ik_m x - i\omega t\right), \tag{1}$$

where the vector function $\mathbf{v}_m$ with respect to y is the cross-sectional velocity distribution for the mth mode and k_m is the wavenumber for the mth mode, both of which are obtained from the plate thickness h and the material constants. The incidence conditions and boundary conditions determine α_m, which is the complex amplitude of the mth mode. In the normal mode expansion technique, Eq. (1) is given by an infinite sum of the Lamb wave modes. The existing modes in a plate always consist of a pair of modes in $\pm x$ directions, owing to the symmetry of a plate, and the sign of the group velocity and the sign of the imaginary part of the wavenumber k_m determine the direction of the waves. In the SAFE technique, the cross section of a plate is divided into layered elements, as shown in Fig. 1, and the nodal displacements and interpolation function yield an eigenequation. Solving the eigenequation gives an approximation of the Lamb waves as a finite sum of their eigenmodes, expressed by Eq. (1).[33] Suppose that $2N$ modes are assigned as $m = 1$ to N for positive propagating or decaying modes ($+x$ modes) and $m = -N$ to -1 for negative propagating or decaying modes ($-x$ modes), and

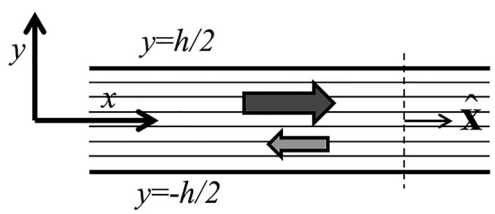

FIG. 1. Lamb waves propagating in a plate.

suppose that the $\pm M$th modes are a pair of $\pm x$ modes. The following equation is satisfied for the wavenumbers:

$$k_M = -k_{-M}. \tag{2}$$

Equation (1) can be expressed as the sum of $+x$ and $-x$ modes as follows:

$$\begin{aligned}\mathbf{v}(x,y) &= \sum_{\substack{m=-N \\ m\neq 0}}^{N} \alpha_m \mathbf{v}_m \exp\left(ik_m x - i\omega t\right) \\ &= \sum_{M=1}^{N} \alpha_M \mathbf{v}_M \exp\left(ik_M x - i\omega t\right) \\ &\quad + \sum_{M=1}^{N} \alpha_{-M} \mathbf{v}_{-M} \exp\left(-ik_M x - i\omega t\right).\end{aligned} \tag{3}$$

Similarly, a stress tensor[36] can be written as follows:

$$\mathbf{T}(x,y) = \sum_{\substack{m=-N \\ m\neq 0}}^{N} \alpha_m \mathbf{T}_m \exp\left(ik_m x - i\omega t\right), \tag{4}$$

where $\mathbf{T}_m$ is the stress distribution tensor for the mth mode and is a function of y that is determined by the plate thickness and material constants, such as $\mathbf{v}_m$.

The time-averaged energy flow per unit time (power) on the cross section in the direction normal to $\hat{\mathbf{x}}$ is represented as follows:[36]

$$P = -\frac{1}{4}\left[\int_{-h/2}^{h/2} \left(\mathbf{v}^* \cdot \mathbf{T} + \mathbf{v} \cdot \mathbf{T}^*\right) \cdot \hat{\mathbf{x}} dy\right], \tag{5}$$

where * denotes the complex conjugate. Substituting Eqs. (3) and (4) into Eq. (5) and rearranging the resulting equation yields the following:

$$P = \sum_{\substack{m=-N \\ m\neq 0}}^{N} \sum_{\substack{n=-N \\ n\neq 0}}^{N} \alpha_m \alpha_n^* P_{mn} \exp\left\{i(k_m - k_n^*)x\right\}, \tag{6}$$

where

$$P_{mn} = -\frac{1}{4}\left[\int_{-h/2}^{h/2} \left(\mathbf{v}_n^* \cdot \mathbf{T}_m + \mathbf{v}_m \cdot \mathbf{T}_n^*\right) \cdot \hat{\mathbf{x}} dy\right]. \tag{7}$$

The characteristics of P_{mn} are described in Ref. 36. The orthogonal relation yields

$$P_{mn} = 0 \quad (k_m \neq k_n^*). \tag{8}$$

Moreover, for propagating modes with real wavenumbers, the symmetry of the propagating modes yields

$$P_{-m,-m} = -P_{mm} \quad (\text{propagating mode}). \tag{9}$$

For non-propagating modes with pure imaginary wavenumbers,

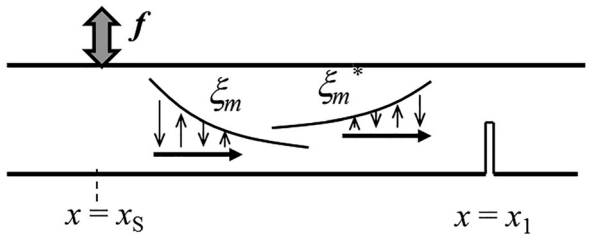

FIG. 2. Coupling of non-propagation modes in the vicinity of incident and reflection points.

$$P_{-mm} = P_{m,-m} \quad (k_m : \text{pure imaginary}). \tag{10}$$

By letting the nth mode satisfying $k_m = k_n^*$ be m^*, Eq. (6) becomes

$$P = \sum_{\substack{m=-N \\ m\neq 0}}^{N} (\alpha_m \alpha_{m^*}{}^* P_{mm^*}). \tag{11}$$

If the mth mode is a propagating mode with a real wavenumber, then $m^* = m$, which implies that the propagating mode m transports energy by interacting only with itself and not with any other modes. If the mth mode is a non-propagating mode with a complex wavenumber, it transports energy by interacting with the m^* th mode that satisfies $k_m = k_{m^*}^*$. The non-propagating modes m and m^* are decaying modes in the $\pm x$ directions, with identical real parts of wavenumbers, as shown in Fig. 2. Because the non-propagating modes can exist only in the vicinity of incident and reflection points, the energy transportation by the interaction of the non-propagating modes occurs only when the incident and reflection points or multiple reflection points are located close to each other.

Next, we consider a plate in which an incident point and a vertical crack are located at $x = x_s$ and $x = x_1$, respectively, as shown in Fig. 3. Although the geometries and material constants have to be uniform in the longitudinal direction in a single SAFE region, a non-volume vertical crack can be modeled by connecting two SAFE regions.[30,31] A crack opening and a connecting junction are expressed by the boundary conditions of zero nodal forces and the continuities of nodal displacements and nodal forces at the junction, respectively. The incident, reflected, and transmitted waves that exist in each region can be expressed as follows:

$$\mathbf{v}^{I-} = \sum_{m=1}^{N} \alpha_m^{I-} \mathbf{v}_{-m} \exp(ik_{-m}x - i\omega t) \quad x < x_S, \tag{12a}$$

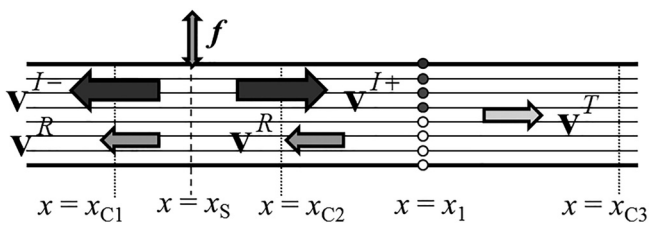

FIG. 3. Positions of an incident source, a vertical crack, and cross-sections for calculating energies in the SAFE method.

$$\mathbf{v}^{I+} = \sum_{m=1}^{N} \alpha_m^{I+} \mathbf{v}_m \exp(ik_m x - i\omega t), \quad x_S < x < x_1, \tag{12b}$$

$$\mathbf{v}^{R} = \sum_{m=1}^{N} \alpha_m^{R} \mathbf{v}_{-m} \exp(ik_{-m}x - i\omega t), \quad x < x_1, \tag{12c}$$

$$\mathbf{v}^{T} = \sum_{m=1}^{N} \alpha_m^{T} \mathbf{v}_m \exp(ik_m x - i\omega t), \quad x > x_1, \tag{12d}$$

where $\mathbf{v}^{I\pm}$, $\mathbf{v}^R$, and $\mathbf{v}^T$ are the velocity vectors of the incident wave in the $\pm x$ directions, the reflected wave, and the transmitted wave, respectively, and α_m denotes a complex amplitude of the mth mode. The incident conditions at $x = x_S$ determine the incident amplitude, $\alpha_m^{I\pm}$. The reflection and transmission amplitudes, α_m^R and α_m^T, are calculated from simultaneous equations formulated by the continuities of nodal displacements and forces at $x = x_1$.[30,31]

Similarly, if the stress tensors are expressed as follows:

$$\mathbf{T}^{I-} = \sum_{m=1}^{N} \alpha_m^{I-} \mathbf{T}_{-m} \exp(ik_{-m}x - i\omega t), \quad x < x_S, \tag{13a}$$

$$\mathbf{T}^{I+} = \sum_{m=1}^{N} \alpha_m^{I+} \mathbf{T}_m \exp(ik_m x - i\omega t), \quad x_S < x < x_1, \tag{13b}$$

$$\mathbf{T}^{R} = \sum_{m=1}^{N} \alpha_m^{R} \mathbf{T}_{-m} \exp(ik_{-m}x - i\omega t), \quad x < x_1, \tag{13c}$$

$$\mathbf{T}^{T} = \sum_{m=1}^{N} \alpha_m^{T} \mathbf{T}_m \exp(ik_m x - i\omega t), \quad x > x_1, \tag{13d}$$

substituting Eqs. (12d) and (13d) into Eq. (5) yields the energy per unit time at $x = x_{c3}$, expressed as follows:

$$P^T = \sum_{m=1}^{N}\sum_{n=1}^{N} \alpha_m^T \alpha_n^{T*} P_{mn} \exp\{i(k_m - k_n^*)x_{C3}\}, \quad x_{C3} > x_1. \tag{14}$$

Because the mode in the $-x$ direction does not exist in the range of $m = 1$ to N and $n = 1$ to N, $n = m^* = m$ holds for $P_{mn} \neq 0$. Consequently, the transmission energy consists only of the interaction of the propagating modes, expressed as follows:

$$P^T = \sum_{\substack{m=1 \\ \text{propagating mode}}}^{N} \alpha_m^T \alpha_m^{T*} P_{mm} \quad x > x_1. \tag{15}$$

This form is independent of x_{C3}.

Next, we consider a cross section $C1$ at $x = x_{C1} < x_S$, where only waves in the $-x$ direction exist, and a velocity vector and a stress tensor are given as a sum of reflected and incident waves, such as $\mathbf{v}^R + \mathbf{v}^{I-}$ and $\mathbf{T}^R + \mathbf{T}^{I-}$. The time-averaged cross-sectional energy flow per unit time is expressed in the form of Eq. (15) as follows:

$$P^{R\&I-} = \sum_{\substack{m=1 \\ \text{propagating mode}}}^{N} (\alpha_m^{I-} + \alpha_m^R)(\alpha_m^{I-} + \alpha_m^R)^* P_{-m-m}, \quad x < x_S. \tag{16}$$

Finally, we consider the cross section $C2$ at $x_S < x_{C2} < x_1$. Because the velocity vector and the stress tensor in the range are given as $\mathbf{v}^R + \mathbf{v}^{I+}$ and $\mathbf{T}^R + \mathbf{T}^{I+}$, substituting them into Eq. (5) yields the time-averaged cross-sectional energy flow per unit time as follows:

$$P^{R\&I+} = P^{I+} + P^R + P^{\text{Non–pro}}, \quad x_S < x < x_1, \tag{17}$$

where P^{I+}, P^R, and $P^{\text{Non–pro}}$ are derived using the relationships for P_{mn} and k_m, given by Eqs. (2), (8), (9), and (10), as follows:

$$P^{I+} = \sum_{\substack{m=1 \\ \text{propagating mode}}}^{N} \alpha_m^{I+} \alpha_m^{I+*} P_{mm}, \tag{18a}$$

$$P^{R} = \sum_{\substack{m=1 \\ \text{propagating mode}}}^{N} \alpha_m^{R} \alpha_m^{R*} P_{-m-m}, \tag{18b}$$

$$P^{\text{Non–pro}} = \sum_{m=1}^{N}\sum_{n=1}^{N} [\alpha_m^R \alpha_n^{I+*} P_{-mn} \exp\{i(k_{-m} - k_n^*)x_{C2}\} - \alpha_n^{R*} \alpha_m^{I+} P_{n,-m} \exp\{i(k_n - k_{-m}^*)x_{C2}\}]. \tag{18c}$$

Note that P_{-mn} and $P_{n,-m}$ in Eq. (18c) are non-zero only when the combination of m and n satisfies $-m = n^*$ from Eq. (8). Then because $k_{-m} = k_n^*$ holds, Eq. (18c) becomes

$$P^{\text{Non–pro}} = \sum_{\substack{n=1 \\ -n^* > 0}}^{N} (\alpha_{-n^*}^{R*} \alpha_n^{I+*} P_{n^*n} + \alpha_n^{R^*} \alpha_{-n^*}^{I+} P_{nn^*}). \tag{19}$$

Here, because $m(= -n^*)$ is a positive integer from 1 to N, the condition of $m(= -n^*) > 0$ is added in the summation of Eq. (19). This implies that only non-propagating modes are considered and that Eq. (19) gives the energy due to the interaction of the non-propagating modes. Note that P^{I+} in Eq. (18a) is the energy generated by external loading at $x = x_S$ and corresponds to the incident energy for an intact plate. Furthermore, P^R is the energy of the reflected waves generated at the crack.

The effect of non-propagating modes (evanescent waves) at plate ends and cracks have been presented in many publications.[19–24,36–44] Bobrovnitiskii[40] described the generation of energy flow caused by the interactions of positive and negative non-propagating modes. Yan and Yuan[41] stated that the propagating energy converted from evanescent waves at a plate edge has the potential for use in nondestructive testing (NDT) of defects and structural health monitoring through power flow analysis. An and Sohn[42] demonstrated experimentally that surface cracks can be detected by measuring displacement enhancement near cracks due to the generation of evanescent waves. Recently, in electromagnetic and ultrasonic studies, the characteristics of evanescent waves have been applied to super-resolution imaging[43,44] in which the resolution of an image exceeds the limitation of the wavelength.

III. RELATIONSHIP BETWEEN SOURCE POSITION AND ENERGY GENERATED

A. Calculation of incident, reflected, and transmitted energy by the SAFE method

This section describes an examination of the energy generated by laser emission to a thin plate with the E-camera using the SAFE method. Elastic waves are generated in a solid medium by a laser through one of two mechanisms: ablation or the thermoelastic effect.[42–53] For large pulse energy, a sudden laser energy input induces plasma emission from the surface of a material, and a normal force is instantaneously loaded as a reaction force of the plasma emission.[45,50] For small laser pulse energy, below the ablation regime, sudden thermal expansion of the surface of a material generates elastic waves.[45,48,49,51–56] Here, considering the two generation mechanisms, elastic wave energy is discussed for point normal loading and dipole loading, as shown in Fig. 4. In the SAFE calculation, a harmonic point force is applied in the y direction to the upper nodal line at $x = x_S$ for normal loading, and dipole nodal force is applied in the $\pm x$ directions to the upper nodal line at two points separated by a distance of $h/100$ for dipole loading. The material used in this study was an aluminum alloy with longitudinal and transverse velocities of $c_L = 6300$ m/s and $c_T = 3100$ m/s.

B. Point normal loading

First, we consider point normal loading [Fig. 4(a)]. Figure 5 shows variations in the elastic wave energy generated for various distances between the point source and the crack, $x_1 - x_S$. The vertical axes of the graphs represent the ratio of the sum of the energy propagating toward the right and left, $P^T + (-P^{R\&I-})$, to the sum of the energy propagating in both directions in a plate without cracks, $P^{I+} + (-P^{I-})(= 2P^{I+})$. Naturally, the ratio is 1.0 for an intact plate. The crack considered here is a non-volume vertical crack with a depth of d.

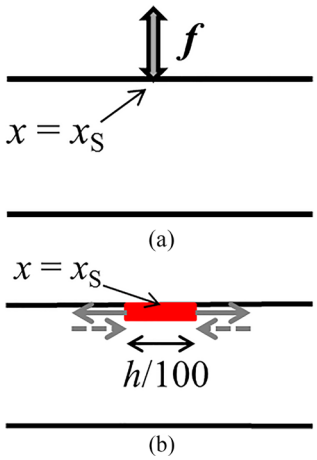

FIG. 4. (Color online) Calculation models used in the SAFE method for the two mechanisms of elastic wave generation by laser. (a) Point normal loading (ablation regime), (b) dipole loading (thermoelastic regime).

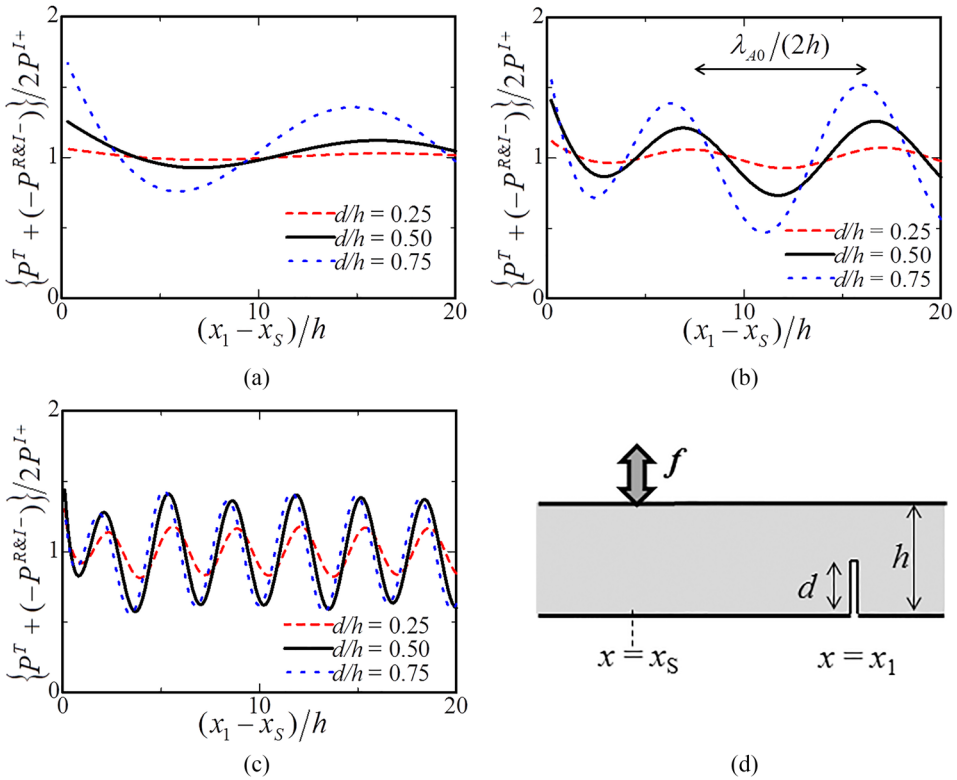

FIG. 5. (Color online) Variations in elastic wave energy generated for various distances between the point normal source and the crack. The crack opening and the point normal source are located on opposite sides; nearly identical curves were obtained when they were located on the same surface. (a) $fh = 5$ kHz mm, (b) $fh = 25$ kHz mm, (c) $fh = 200$ kHz mm, (d) source and crack arrangement.

The dotted blue, solid black, and dashed red lines represent $d/h = 0.25$, 0.50, and 0.75, respectively. Figures 5(a)–5(c) shows the curves obtained when the crack opening is located opposite the incident surface, as shown in Fig. 5 (d). These curves are nearly identical to those obtained when the crack opening and the incident source are located on the same side. Figures 5(a)–5(c) show the curves obtained at different frequency–thickness products (fh). Here, $fh = 25$ kHz mm corresponds to the value used in the fundamental work on the E-camera,[17,18] whereas $fh = 5$ kHz mm and $fh = 200$ kHz mm are examples of lower- and higher-frequency–thickness products. Because the A1 cutoff frequency is $fh = 1550$ kHz mm for the aluminum alloy plate used in this study, the propagating modes are only the A0 and S0 modes for these fh values.

In all cases, as Figs. 5(a)–5(c) show, the energy ratios periodically vary around 1.0 in the normalized distance range of $(x_1 - x_S)/h > 5$. The interference of the reflected wave $\mathbf{v}^R$ and the incident wave in the $-x$ direction, $\mathbf{v}^{I-}$, causes energy variations whose periods correspond to half of the normalized wavelength of the A0 mode, $\lambda_{A0}/(2h) = 22.0$, 9.8, and 3.3, at the fh values. When the incident source is located in the vicinity of the crack, i.e., $(x_1 - x_S)/h > 5$, the energy ratios tend to be greater than 1.0, and the maximum values become larger as the crack depth d/h increases. In other words, even if the external loading is constant, a large amount of vibration energy is generated when an incident source is located close to a crack, compared to the energy ratio of 1.0 for incidence at intact areas, and the maximum value corresponds to the depth of the crack.

C. Dipole loading

This section discusses variations in the elastic wave energy for dipole loading, as illustrated in Fig. 4(b). Figures 6(a)–6(c) show the energy variations for various distances between the center of the dipole source and the crack located opposite the source, as shown in Fig. 6(d), for different fh values at depths $d/h = 0.25$, 0.50, and 0.75. As in Fig. 5, the energy ratios vary around 1.0 at large $(x_1 - x_S)/h$. This also causes interference of the reflected wave $\mathbf{v}^R$ and the incident wave $\mathbf{v}^{I-}$. Figure 6(c) shows a complex variation at large $(x_1 - x_S)/h$, unlike the monotonous variations seen in Figs. 5(a)–5(c) and Figs. 6(a) and 6(b). This is because two modes with different wavelengths, i.e., A0 and S0, are generated and interfere in the fh range. In the vicinity of $(x_1 - x_S)/h = 0$, the energy abruptly increases in all cases. To show the small range of $(x_1 - x_S)/h$ clearly, magnified views are shown in the insets. The energy curves abruptly increase in the vicinity of $(x_1 - x_S)/h = 0$, compared with normal loading, and exhibit a similar trend in that the maximum energy increases with the crack depth.

Figures 7(a)–7(c) shows the energy variations when the crack opening and the dipole source are on the same surface, as shown in Fig. 7(d). As in Figs. 5 and 6, the energy variations are shown for different fh values and crack depths. As the dipole source moves closer to the crack opening, the energy approaches zero; this behavior is completely different from that seen in Fig. 6. The energy generation mechanism in dipole loading (the thermoelastic effect) causes zero energy generation at $(x_1 - x_S)/h = 0$. When the dipole source is close to the crack opening with a traction-free boundary, as show in Fig. 8, an incident stress wave heading toward the crack generates a phase-inverted reflected wave at the crack opening. If the dipole source is sufficiently close to the crack, the incident wave propagated from the left edge of the dipole source in the left direction and the reflected

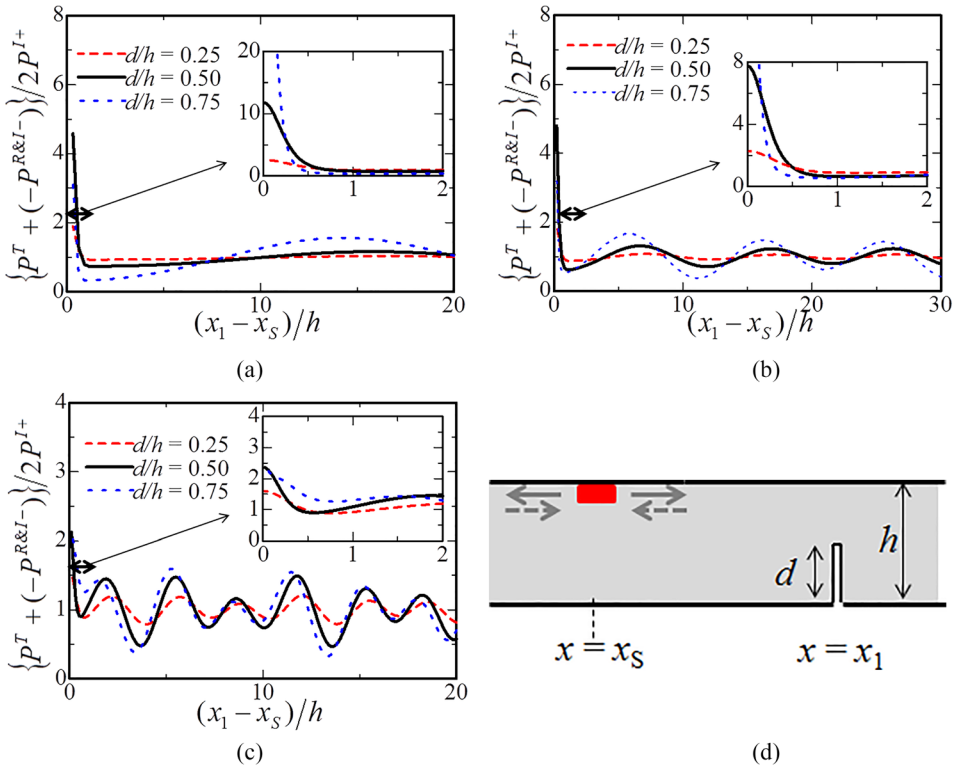

FIG. 6. (Color online) Variation in elastic wave energy generated for various distances between the dipole source and the crack. The crack opening is opposite to the incident source. (a) $fh = 5$ kHz mm, (b) $fh = 25$ kHz mm, (c) $fh = 200$ kHz mm, (d) source and crack arrangement.

wave are cancelled out; consequently, the generated energy becomes zero at $(x_1 - x_S)/h = 0$.

D. Modal analysis of generation energy

From the results presented above, we can conclude that the generated energy varies significantly when the incident source is located in the vicinity of the crack. This trend can be explained using the energy equations presented in Sec. II. Note that $P^{R\&I+}$ in Eq. (17) represents the energy passing through the cross section between the incident source and the crack, whereas P^R denotes the reflected waves heading away from the crack. Therefore, $P^{I+} + P^{\text{Non–pro}}$ represents the energy heading toward the crack. Because P^{I+} denotes the incident energy for a plate without cracks, $P^{\text{Non–pro}}$ denotes the energy increment due to the existence of a crack.

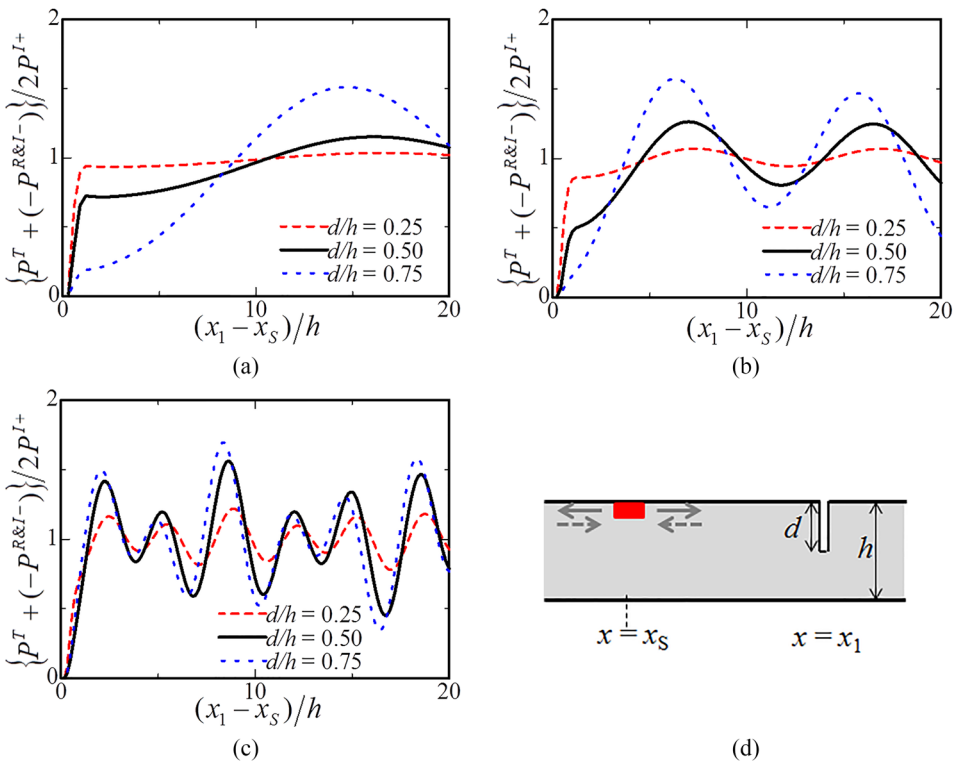

FIG. 7. (Color online) Variation in elastic wave energy generated for various distances between the dipole source and the crack. The crack opening and the incident source are on the same surface. (a) $fh = 5$ kHz mm, (b) $fh = 25$ kHz mm, (c) $fh = 200$ kHz mm, (d) source and crack arrangement.

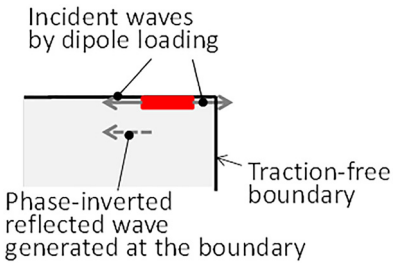

FIG. 8. (Color online) Schematic of stress waves by dipole loading (thermal expansion) in the vicinity of a crack opening and a reflected stress wave.

As $P^{\text{Non–pro}}$ depends only on the non-propagating modes, the energy increases only when the incident source and the crack are close.

This section considers the energy for each mode in the energy increment $P^{\text{Non–pro}}$ using the characteristic of the SAFE method, whereby the velocity and stress fields can be calculated for each mode. Figure 9 shows the normalized energy increment $P^{\text{Non–pro}}/P^{I+}$ versus the normalized distance between the incident source and a crack $(x_1 - x_S)/h$ for normal incidence opposite the crack opening at $fh = 25$ kHz mm and $d/h = 0.5$, corresponding to the black line in Fig. 5(b). Because $P^{I+} + P^{\text{Non–pro}}$ represents the energy transported from the incident source to the crack, we cannot see the periodic energy variation caused by the interference of the reflected wave $\mathbf{V}^R$ and the incident wave propagating in the $-x$ direction, $\mathbf{V}^{I-}$, as seen in Figs. 5–7. In other words, $P^{\text{Non–pro}}$ denotes a substantial energy increment owing to the existence of cracks. Figure 9 shows the case of normal incidence opposite the crack opening; the curves obtained are nearly identical to those obtained when the crack opening and the incident source are located on the same side.

The dashed blue line represents the energy of the A1 mode, P^{A1-A1}/P^{I+}, included in $P^{\text{Non–pro}}/P^{I+}$. The interaction of the A1 mode of the incident wave and the A1 mode of the reflected wave generates P^{A1-A1}, where the A1 modes have pure imaginary wavenumbers at the fh value. The dashed blue line is exactly the same as the solid black line denoting $P^{\text{Non–pro}}/P^{I+}$, which implies that the energy increment $P^{\text{Non–pro}}$ consists only of the contribution of the A1 mode, P^{A1-A1}.

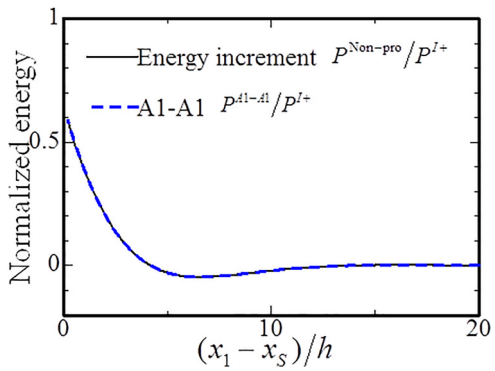

FIG. 9. (Color online) Total energy increment $P^{\text{Non–pro}}/P^{I+}$ and A1 mode-coupled energy for point normal loading.

Figure 10 shows the energy increment $P^{\text{Non–pro}}/P^{I+}$ for dipole loading when the crack opening and the dipole source are (a) on the opposite side and (b) on the same side ($fh = 25$ kHz mm, $d/h = 0.5$). The solid black lines represent the total energy increment $P^{\text{Non–pro}}/P^{I+}$, whereas the solid blue, solid red, dashed blue, and dashed red lines represent the mode-coupled energy of A1–A1, A2–A3, S1–S2, and S2–S1, respectively. They imply that the total energy increment consists of the energies of the higher-order modes as well as the energy of the A1 mode. Because the higher-order modes exert an influence only in the immediate vicinity of the crack, the energy increment abruptly increases at $(x_1 - x_S)/h = 0$.

IV. EXPERIMENTAL VERIFICATION FOR DIPOLE LOADING

To verify the energy variations in the vicinity of a crack experimentally, defect images were obtained using the E-camera system and an aluminum alloy plate, as shown in Fig. 11. Artificial straight notches with a length of 50 mm, width of 1.0 mm, and depth of 1.5 mm were engraved on a single surface of a plate measuring 500 mm $\times$ 500 mm $\times$ 3.0 mm. Because the notch width of 1.0 mm was sufficiently small in comparison to the wavelength of the flexural wave used in this study, the notch was regarded as a non-volume crack in the SAFE calculations described in Secs. II and III. The laser was scanned over a region of 400 mm $\times$ 40 mm at 1.0-mm intervals to obtain images of all the notches and a region of 80 mm $\times$ 40 mm at 0.5-mm

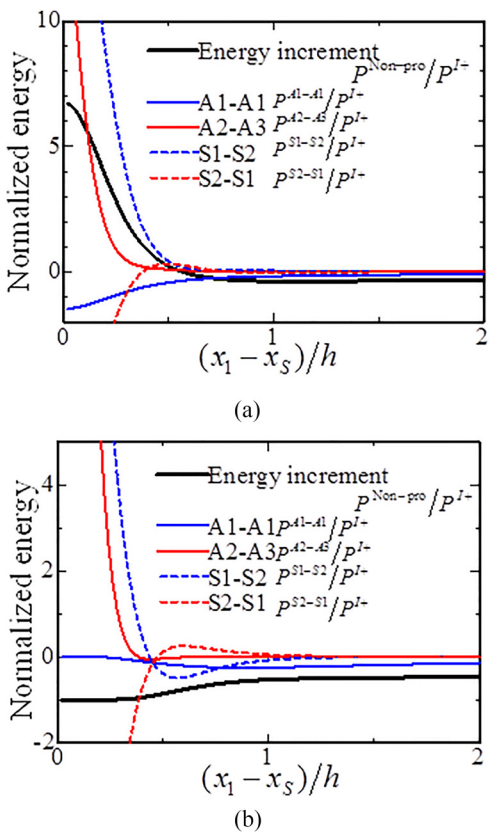

FIG. 10. (Color online) Total energy increment $P^{\text{Non–pro}}/P^{I+}$ and mode coupled energy for dipole loading. (a) Opposite side, (b) same side.

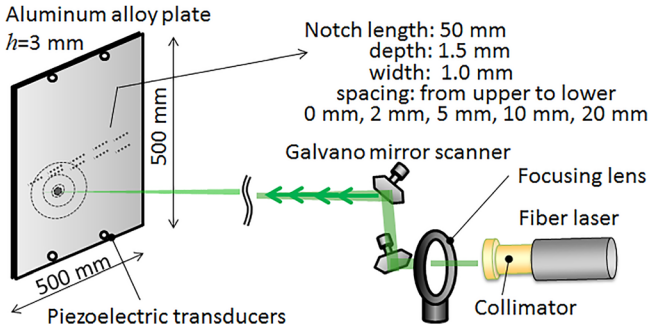

FIG. 11. (Color online) Experimental set-up and specimen used.

intervals to obtain an image of a single notch. Because a repetition frequency of 20 Hz was used to avoid the occurrence of spurious images,[17,18] the measurement times were approximately 14 min for the region 400 mm × 40 mm in size (401 × 41 points) and approximately 11 min for the region 80 mm × 40 mm in size (161 × 81 points). The E-camera system has been described in detail in previous studies.[17,18] A tone burst wave of 8 kHz was generated by modulating the pulse trains of a fiber laser. A laser spot with a diameter of approximately 0.5 mm was focused using a collimator and a focusing lens. In the current study, piezoelectric transducers with a central frequency of 8 kHz were used as receiving devices to detect non-averaged signals at a high signal-to-noise ratio. The four piezoelectric devices attached to the plate received the elastic waves generated at the laser spots. The peak distribution of the Fourier spectra of the received signals was obtained for each receiver, and the average of the four distributions was regarded as a defect image.[14,16–18] References 14 and 16 provide more information on the process of averaging the distributions.

Figure 12 shows the defect images when the laser beam was irradiated on the plate surface opposite the crack opening. In both (a) the wide-range image and (b) the zoomed image, darker regions are located at the notches and in the vicinity of the notches. The dark areas other than the notches are resonance patterns induced by the interference between the incident and reflected waves, as seen in Figs. 5–7. Because the experimental system used in this study does not

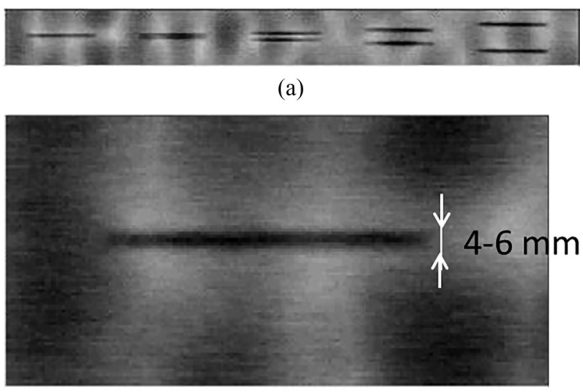

(a)

(b)

FIG. 12. Defect images when the laser beam was irradiated on the plate surface opposite to the crack opening. (a) Wide-range image (400 × 40), (b) zoomed image (80 × 40).

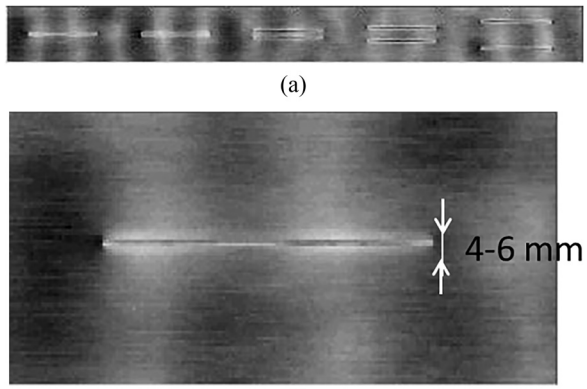

(a)

(b)

FIG. 13. Defect images when laser beam was irradiated on the same surface as the crack opening. (a) Wide-range image (400 × 40), (b) zoomed image (80 × 40).

damage plate surfaces, the thermoelastic effect is dominant for the generated elastic wave. The dark band shown in the zoomed image [Fig. 12(b)] ranges from 4 to 6 mm in width. This is in good agreement with the results for dipole loading shown in Figs. 6(b) and 10(a), where the large energy range becomes less than the plate thickness h (= 3.0 mm in the experiment).

Figure 13 shows (a) a wide-range image and (b) a zoomed image obtained when the laser beam was irradiated on the same surface as the crack opening. In both images, darker lines appear at the center of the notches because the laser beam enters into the notches, and the vicinity of the cracks appears brighter. The brighter regions range from approximately 4 mm to 6 mm in width, which is in good agreement with Figs. 7(b) and 10(b).

Thus, the energy variations in the vicinity of a crack, as shown in Figs. 6, 7, and 10, have been verified experimentally. Using the calculation results presented in Sec. III, we can predict the energy variations from the frequency range, plate thickness, and elastic wave generation mechanism. Accordingly, we can determine suitable settings of the E-camera, such as the frequency range and scan pitch, to achieve desired defects.

V. CONCLUSIONS

The cross-sectional energies of a plate were calculated by the semi-analytical finite element (SAFE) method to elucidate the principle of imaging for a plate using a scanning laser source (E-camera). The results may be summarized as follows.

(1) The cross-sectional energies generated in a plate vary significantly when an incident source is located in the vicinity of a crack.
(2) In point normal loading in the fh ranges considered in this study, the generated energies became larger in the vicinity of a crack in both cases, i.e., when the crack opening and the incident source are located on the same side and when they are located on opposite sides. This causes an energy increment due to the non-propagating A1 modes.

(3) In dipole loading, when the crack opening and the dipole source are located on opposite sides, the generated energy abruptly increases in the vicinity of a crack, which is affected by higher-order non-propagating modes as well as the A1 mode.
(4) In dipole loading, when the crack opening and the dipole source are located on the same side, the generated energy decreases in the vicinity of a crack. This is because the phase-inverted reflected wave and incident wave are canceled out.

Defect imaging experiments conducted using the E-camera system demonstrated points (3) and (4) stated above. Using the knowledge obtained in this study, we can determine suitable settings of the E-camera to achieve desired defects.

ACKNOWLEDGMENTS

This work was supported by JSPS KAKENHI Grant No. 26282094 and Chubu Electric Power Co., Inc.

[1]I. A. Victorov, *Rayleigh and Lamb Waves* (Plenum, New York, 1967), Chap. III, pp. 123–144.
[2]J. L. Rose, *Ultrasonic Waves in Solid Media* (Cambridge University Press, New York, 1999), Appendix E, pp. 400–438.
[3]D. N. Alleyne, M. J. S. Lowe, and P. Cawley, "The reflection of guided waves from circumferential notches in pipes," J. Appl. Mech. **65**, 635–641 (1998).
[4]D. N. Alleyne, B. Pavlakovic, M. J. S. Lowe, and P. Cawley, "Rapid long-range inspection of chemical plant pipework using guided waves," Insight **43**, 93–96, 101 (2001).
[5]P. J. Mudge, "Field application of the Teletest (R) long-range ultrasonic testing technique," Insight **43**, 74 (2001).
[6]P. Cawley, M. J. S. Lowe, D. N. Alleyne, B. Pavlakovic, and P. Wilcox, "Practical long range guided wave testing: Applications to pipes and rails," Mater. Eval. **61**, 66–74 (2003).
[7]H. Kwun, S. Y. Kim, and G. M. Light, "The magnetostrictive sensor technology for long range guided wave testing and monitoring of structures," Mater. Eval. **61**, 80–84 (2003).
[8]R. Sicard, A. Chahbaz, and J. Goyette, "Guided lamb waves and L-SAFT processing technique for enhanced detection and imaging of corrosion defects in plates with small depth-to-wavelength ratio," IEEE Trans. Ultrason. Ferroelectr. Freq. Control **51**, 1287–1297 (2004).
[9]T. Hayashi and M. Murase, "Defect imaging with guided waves in a pipe," J. Acoust. Soc. Am. **117**, 2134–2140 (2005).
[10]T. Hayashi, M. Nagao, and M. Murase, "Defect imaging with guided waves in a long pipe," J. Solid Mech. Mater. Eng. **2**, 888–899 (2008).
[11]J. Ma and P. Cawley, "Low-frequency pulse echo reflection of the fundamental shear horizontal mode from part-thickness elliptical defects in plates," J. Acoust. Soc. Am. **127**, 3485–3593 (2010).
[12]J. Davies and P. Cawley, "The application of synthetic focusing for imaging crack-like defects in pipelines using guided waves," IEEE Trans. Ultrason. Ferroelectr. Freq. Control **56**, 759–771 (2009).
[13]T. Hayashi, M. Murase, and M. N. Salim, "Rapid thickness measurements using guided waves from a scanning laser source," J. Acoust. Soc. Am. **126**, 1101–1106 (2009).
[14]T. Hayashi, M. Murase, and T. Kitayama, "Frequency dependence of images in scanning laser source technique for a plate," Ultrasonics **52**, 636–642 (2012).
[15]M. N. Salim, T. Hayashi, M. Murase, T. Ito, and S. Kamiya, "Fast remaining thickness measurement using a laser source scanning technique," Mater. Trans. **53**, 610–616 (2012).
[16]T. Hayashi, M. Murase, N. Ogura, and T. Kitayama, "Imaging defects in a plate with full non-contact scanning laser source technique," Mater. Trans. **55**, 1045–1050 (2014).
[17]T. Hayashi, "Imaging defects in a plate with complex geometries," Appl. Phys. Lett. **108**, 081901 (2016).
[18]T. Hayashi and M. Fukuyama "Fast non-contact defect imaging with scanning laser source technique," in *Proceedings of the 19th World Congress on Nondestructive Testing* (2004).
[19]A. K. Kromine, P. A. Fomitchov, S. Krishnaswamy, and J. D. Achenbach, "Laser ultrasonic detection of surface breaking discontinuities: Scanning laser source technique," Mater. Eval. **58**, 173–177 (2000).
[20]Y. H. Sohn and S. Krishnaswamy, "Interaction of a scanning laser-generated ultrasonic line source with a surface-breaking flaw," J. Acoust. Soc. Am. **115**, 172–181 (2004).
[21]Y. Sohn and S. Krishnaswamy, "A near-field scanning laser source technique and a microcantilever ultrasound receiver for detection of surface-breaking defects," Meas. Sci. Technol. **17**, 809–818 (2006).
[22]S. Dixon, B. Cann, D. L. Carroll, Y. Fan, and R. S. Edwards, "Non-linear enhancement of laser generated ultrasonic Rayleigh waves by cracks," Nondestruct. Test. Eval. **23**, 25–34 (2008).
[23]A. R. Clough and R. S. Edwards, "Scanning laser source Lamb wave enhancements for defect characterisation," NDT E Int. **62**, 99–105 (2014).
[24]A. R. Clough and R. S. Edwards, "Characterisation of hidden defects using the near-field ultrasonic enhancement of Lamb waves," Ultrasonics **59**, 64–71 (2015).
[25]P. A. Fomitchov, A. K. Kromin, S. Krishnaswamy, and J. D. Achenbach, "Imaging of damage in sandwich composite structures using a scanning laser source technique," Comp. Part B **35**, 557–562 (2004).
[26]J. Takatsubo, B. Wang, H. Tsuda, and N. Toyama, "Generation laser scanning method for the visualization of ultrasounds propagating on a 3-D object with an arbitrary shape," J. Solid Mech. Mater. Eng. **1**, 1405–1411 (2007).
[27]R. B. Dong and S. B. Nelson, "On natural vibrations and waves in laminated orthotropic plates," J. Appl. Mech. **39**, 739–745 (1972).
[28]R. L. Datta, S. K. Shah, A. H. Bratton, and T. Chakraborty, "Wave propagation in laminated composite plates," J. Acoust. Soc. Am. **83**, 2020–2026 (1988).
[29]L. Gavrić, "Computation of propagative waves in free rail using a finite element technique," J. Sound Vib. **185**, 531–543 (1995).
[30]G. R. Liu and J. D. Achenbach, "Strip element method for stress analysis of anisotropic linearly elastic solids," J. Appl. Mech. **62**, 607–613 (1995).
[31]T. Hayashi and K. Kawashima, "Multiple reflections of Lamb waves at a delamination," Ultrasonics **40**, 193–197 (2002).
[32]T. Hayashi, K. Kawashima, Z. Sun, and J. L. Rose, "Analysis of flexural mode focusing by a semianalytical finite element method," J. Acoust. Soc. Am. **113**, 1241–1248 (2003).
[33]T. Hayashi, W.-J. Song, and J. L. Rose, "Guided wave dispersion curves for a bar with an arbitrary cross-section, a rod and rail example," Ultrasonics **41**, 175–183 (2003).
[34]T. Hayashi, C. Tamayama, and M. Murase, "Wave structure analysis of guided waves in a bar with an arbitrary cross-section," Ultrasonics **44**, 17–24 (2006).
[35]K. F. Graff, *Wave Motion in Elastic Solids* (Dover, New York, 1991), Chap. 8, pp. 431–581.
[36]B. A. Auld, *Acoustic Fields and Waves in Solids I, II*, 2nd ed. (Krieger, Malabar, 1990), Chap. 10, pp. 63–220.
[37]M. Castaings, E. Le Clezio, and B. Hosten, "Modal decomposition method for modeling the interaction of Lamb waves with cracks," J. Acoust. Soc. Am. **112**, 2567–2582 (2002).
[38]B. Morvan, N. Wilkie-Chancellier, H. Duflo, A. Tinel, and J. Duclos, "Lamb wave reflection at the free edge of a plate," J. Acoust. Soc. Am. **113**, 1417–1425 (2003).
[39]O. Diligent, M. J. S. Lowe, E. Le Clézio, M. Castaings, and B. Hosten, "Prediction and measurement of nonpropagating Lamb modes at the free end of a plate when the fundamental antisymmetric mode A0 is incident," J. Acoust. Soc. Am. **113**, 3032–3042 (2003).
[40]Y. I. Bobrovnitskii, "On the energy flow in evanescent waves," J. Sound Vib. **152**, 175–176 (1992).
[41]X. Yan and F.-G. Yuan, "Conversion of evanescent Lamb waves into propagating waves via a narrow aperture edge," J. Acoust. Soc. Am. **137**, 3523–3533 (2015).
[42]Y.-K. An and H. Sohn, "Visualization of non-propagating Lamb wave modes for fatigue crack evaluation," J. Appl. Phys. **117**, 114904 (2015).
[43]F. Simonetti, "Multiple scattering: The key to unravel the subwavelength world from the far-field pattern of a scattered wave," Phys. Rev. E **73**, 036619 (2006).

[44]S. Lani, K. G. Sabra, and F. L. Degertekin, "Super-resolution ultrasonic imaging of stiffness variations on a microscale active metasurface," Appl. Phys. Lett. **108**, 084104 (2016).
[45]C. B. Scruby and L. E. Drain, *Laser Ultrasonics: Techniques and Applications* (Adam Hilger, New York, 1990), Chap. 5, pp. 223–324.
[46]J.-C. Cheng and Y. H. Berthelot, "Theory of laser-generated transient Lamb waves in orthotropic plates," J. Phys. D **29**, 1857–2867 (1996).
[47]T. Sanderson, C. Ume, and J. Jarzynski, "A comparison of Q-switched and intensity modulated laser pulses for ultrasonic NDT," J. Nondestruct. Eval. **17**, 199–208 (1998).
[48]J. D. Achenbach, "Laser excitation of surface wave motion," J. Mech. Phys. Solids **51**, 1885–1902 (2003).
[49]I. Arias and J. D. Achenbach, "Thermoelastic generation of ultrasound by line-focused laser irradiation," Int. J. Solids Struct. **40**, 6917–6935 (2003).
[50]Y. Shi, S.-C. Wooh, and M. Orwat, "Laser-ultrasonic generation of Lamb waves in the reaction force range," Ultrasonics **41**, 623–633 (2003).
[51]B. Xu, Z. Shen, X. Ni, and J. Lu, "Numerical simulation of laser-generated ultrasound by the finite element method," J. Appl. Phys. **95**, 2116–2122 (2004).
[52]J. D. Achenbach, "Simplifications for the calculation of surface wave pulses generated by laser-irradiation," J. Acoust. Soc. Am. **116**, 1481–1487 (2004).
[53]J. D. Achenbach, "The thermoelasticity of laser-based ultrasonics," J. Therm. Stress. **28**, 713–727 (2005).
[54]J. D. Achenbach, "Application of the reciprocity theorem to analyze ultrasound generated by high-intensity surface heating of elastic bodies," J. Therm. Stress. **30**, 841–853 (2007).
[55]I. A. Veres, T. Berer, and P. Burgholzer, "Numerical modeling of thermoelastic generation of ultrasound by laser irradiation in the coupled thermoelasticity," Ultrasonics **53**, 141–149 (2013).
[56]W. Liu and J.-W. Hong, "Modeling of three-dimensional Lamb wave propagation excited by laser pulses," Ultrasonics **55**, 113–122 (2015).